

# Study of cubic and hexagonal cell geometries of a 3D diamond detector with a proton micro-beam

M. J. Booth<sup>1</sup>, G. T. Forcolin<sup>2</sup>, V. Grilj<sup>3</sup>, B. Hamilton<sup>4</sup>, I. Haughton<sup>2</sup>, M. McGowan<sup>4</sup>,  
S. A. Murphy<sup>2</sup>, A. Oh<sup>2\*</sup>, P. S. Salter<sup>1</sup>, I. Sudić<sup>3</sup>, N. Skukan<sup>3</sup>

1. Department of Engineering Science, University of Oxford, UK

2. School of Physics and Astronomy, University of Manchester, UK

3. Ruder Bošković Institute, Zagreb, Croatia

4. School of Electrical and Electronic Engineering, University of Manchester, UK

## Abstract

A detector from single crystal synthetic diamond with conducting wires has been prepared with an improved femto-second laser process. The detector was characterised with a 4.5 MeV proton micro-beam (Ruder Bošković Institute, Zagreb). The charge collection efficiency and the transient current response have been investigated with high spatial resolution. A hexagonal and square cell geometry is investigated. The experimental data is compared to a simulation.

## 1. INTRODUCTION

Diamond detectors with conductive wires in the bulk, so called 3D diamond detectors, have been demonstrated to work as position sensitive, segmented detectors [1], and to exhibit good superior radiation hardness compared to conventional planar diamond detectors [2]. In this study we examine the charge collection properties of a novel generation of 3D diamond detectors fabricated with a femto-second laser and aberration correcting optics.

The paper is structured as follows: Section 2 describes the production process of the 3D diamond test detector. Section 3 presents studies of the charge collection properties with a proton micro beam including spatially resolved transient currents and a comparison of the experimental data to simulation results.

## 2. DETECTOR FABRICATION

To trace out conducting wires in diamond a sufficiently large photon density is needed to achieve non-linear absorption of photons and

in consequence localised phase transition of diamond into a combination of a graphitic phase and amorphous carbon [3].

The conductive wires in the test device are fabricated with a short laser pulse of 100 fs duration at a wavelength of 790 nm and a repetition rate of 1 kHz from an amplified Ti:sapphire laser (SpectraPhysics Solstice), operating in TEM<sub>00</sub> beam mode [4]. Focussing the laser inside the diamond, there is severe spherical aberration due to the refractive index mismatch at the diamond interface, limiting the efficiency of the laser fabrication. To counter this a liquid crystal spatial light modulator (SLM) was employed to adaptively correct for the aberration during fabrication [5], ensuring that a well defined diffraction limited focal spot is achieved inside the diamond. Using aberration correction in the fabrication gives a better yield and improves the wire properties significantly compared to conventional processing [6].

The diamond sample was mounted to a programmable 3-axis stage to control the location of the focal point of the beam within the diamond sample with a fixed translational speed of

\*Corresponding author: alexander.oh@manchester.ac.uk

10  $\mu\text{m}/\text{s}$ . The laser power was adjusted using a using an adjustable half wave plate in conjunction with a polarizer, and the laser beam was focused to a diameter of  $\leq 1 \mu\text{m}$  using an air based objective lens with numerical aperture 0.75.

A single crystal electronic-grade sample obtained from Ila[7], with dimensions  $4.0 \times 4.0 \times 0.4 \text{mm}^3$  was used as substrate. An array of graphitic wires was written into the diamond, arranged such that square, rectangular and hexagonal shaped detector cells were formed. The wires have a diameter of about  $2 \mu\text{m}$ .

A structured metallisation pattern was applied to the front and back side of the sample to provide electrical contacts to the conductive wires. The metallisation was achieved with a sputtering process and consists of a chromium layer of 50 nm thickness providing adhesion to the diamond, and a gold layer of 80 nm thickness to prevent oxidization of the chromium layer. The sample was annealed at  $250^\circ\text{C}$  for 5 minutes in a nitrogen atmosphere.

Three different detector structures have been placed on the sample as shown in Figure 1a: a planar metal strip array for reference; a 3D array consisting of square cells, rectangular cells, and hexagonal cells (Figure 1b) all with  $100 \mu\text{m}$  pitch; and a 3D “phantom” array, i.e. an area where the same metallization pattern used to connect the graphitic wires is applied but without wires, for comparing the charge collected by the metallization alone. Sets of readout electrodes of the 3D structures were ganged together to form strips. The bias electrodes were connected from the opposite side to a common biasing pad. The electrodes exhibit an ohmic behavior until approximately  $\pm 40 \text{V}$ , and show an exponential increase in current for higher voltages. The resistivity has been determined to  $0.7 \pm 0.1 \Omega\text{cm}$ .

The structure of the electrode at the surface was imaged using a Scanning Electron Microscope (SEM) and compared to structures which were fabricated without adaptive optical correction of the spherical aberration. Figure 2 shows both samples exhibit at the end of the conductive wires small craters on the surface where the laser exited the diamond during the processing. The lower density of the electrode material compared to the diamond causes pressure inside the

diamond sample and is sufficiently high to eject a few microns of diamond material at the surface. The two images reveal that aberration correction during fabrication allows a better control on the electrode diameter. A periodic surface structuring can be seen in Figure 2a, which is characteristic of the interaction between a linearly polarized ultrafast laser and the diamond surface [8].

### 3. PROTON TEST BEAM

A proton microbeam [9] at the Ruđer Bošković Institute in Zagreb was used to study the detector by ion beam induced charge (IBIC) and time resolved ion beam induced current (TRIBIC). It is based on a Van-de-Graaff accelerator that can accelerate protons to an energy of 4.5 MeV and produce a micro-beam with an FWHM of  $\leq 2 \mu\text{m}$ . The proton stopping range in diamond is approximately  $97 \mu\text{m}$  at 4.5 MeV [10], thus protons will stop within the detector volume. The spatial distribution of the ionisation charge is estimated using SRIM [10], a software package to simulate ion transport in matter. The FWHM of the charge distribution in the transverse plane is estimated to be less than  $5 \mu\text{m}$  at the stopping distance.

The sample was mounted on a PCB specifically designed for optimised high frequency response. A single strip was wire bonded to a read-out pad (channel 1). The adjacent two strips on either side of the first strip were ganged together and connected to a second read-out pad (channel 2). The bias voltage was connected to the entire detector. The signal lines are connected via SMA connectors to the read-out electronics. For the IBIC measurements the read-out chain consisted of a charge integrating amplifier followed by a shaping amplifier with a shaping time of  $2 \mu\text{s}$ . A self-triggered data acquisition system recorded the amplitude of the charge signal with a trigger threshold of 20ke, as well as the position of the proton beam. For the TRIBIC measurements the read-out chain was modified to record transient currents. The current signal generated by the 4.5 MeV proton was amplified with a Cividec C2 2 GHz broadband current amplifier [11] and digitised with a WaveMaster-8500 5 GHz sampling scope from

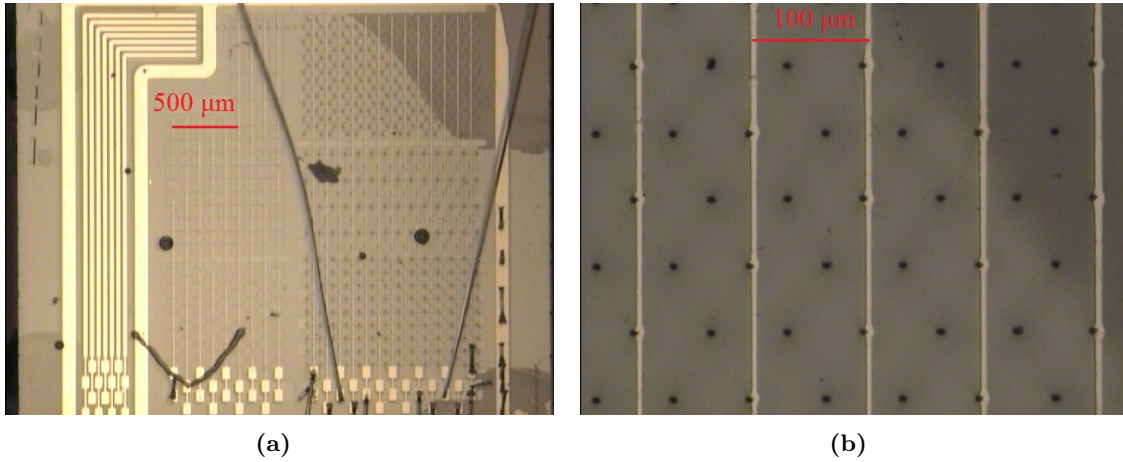


**Figure 1:** Optical images of the detector. The metallisation and readout strips are shown in gold. (a) the three areas are: Left, planar array; Middle, 3D phantom array; Right, 3D array. (b) hexagonal cell array, with the readout strips in gold and shadows of the bias connections for the hexagonal cells also visible.

Lecroy. The waveform and the position of the proton beam was recorded with a self-triggered data acquisition system. The read-out chains were calibrated with a silicon detector assuming an ionisation energy of 3.6 eV per electron-hole pair in silicon.

### 3.1. IBIC Results

The diamond test detector has been characterised in terms of a charge collection efficiency (CCE), defined as the ratio of measured amount of charge from the detector, and the produced amount of charge in the diamond by the ionizing proton. The CCE has been measured as a function of position on the detector with a spatial resolution of a few microns.

The results on the CCE measured on square and hexagonal shaped cell with the proton micro beam are shown in Figure 3. The data obtained with the read-out channel 1 are shown. The shape of the hexagonal and square cells is clearly visible. The conducting wires in the diamond bulk exhibit a lower CCE and show as darker areas. Data taken at a bias voltage of  $U_b = -2$  V show a less sharp boundary between channel 1 and the cells connected to channel 2, while the separation is well defined for  $U_b = -20$  V and the shape of the cells is rendered clearly. With increasing applied bias voltage the CCE both increases and becomes more uniform across the

cell, as can be seen in comparing Figures 3b and 3d to 3a and 3c.

The CCE averaged over data from channel 1 and 2 are shown in Figure 4 as a function of bias voltage,  $U_b$ . No data was recorded in the square array at +40 V due to high leakage current. The measured CCE is consistent for both square and hexagonal cells and symmetric for positive and negative bias voltages, reaching close to full charge collection at  $|U_b| \geq 20$  V.

The charge deposited in the detector by the incident proton can be shared by adjacent cells if the proton impacts in the region of the cell boundary. This ‘charge sharing’ and can be parameterised as follows:

$$\eta = \frac{q_2}{q_1 + q_2} \quad (1)$$

where  $\eta$  is the fraction of the total charge collected by the outer channel 2, and  $q_1$  and  $q_2$  the values of charge collected with channels 1 and 2, respectively. Figure 5 shows the value of  $\eta$  as measured in the square and hexagonal cells at 2 V and 20 V. In averaging over several horizontal slices, a charge sharing width was calculated by taking the width of the 25% to 75% transition of the  $\eta$  value in the cell boundary region. In the case of the hexagonal cell, the tilt of the cell edge was applied before measuring the width. The  $\eta$  transition region at the left and right of the central cell was averaged. The

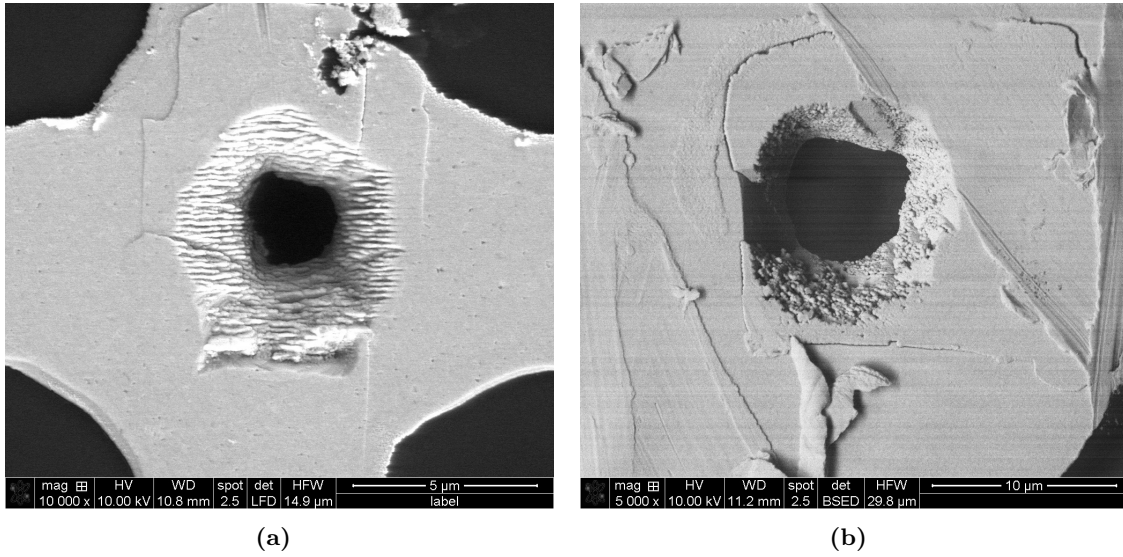


**Figure 2:** A comparison of SEM images for (a) a sample produced with optical aberration correction and (b) a sample produced without correction. The scale of the SEM in (a) is smaller by a factor two compared to (b). The electrode diameter in (a) is significantly smaller due to greater control in the electrode formation.

variation of the charge sharing width as a function of applied bias is shown in Figure 6. The observed charge sharing  $\eta$  is about 25% lower for the hexagonal cells compared to the square cells for the same value of  $U_b$ . The covered area of a single hexagonal and square cell are comparable,  $11500\mu\text{m}^2$  and  $10000\mu\text{m}^2$ , respectively, with the hexagonal cell covering a 15% larger area. The charge sharing region for  $U_b \geq -40\text{V}$  is  $15\mu\text{m}$  for hexagonal and  $22\mu\text{m}$  for cubic cell geometry.

### 3.2. TRIBIC Measurements and Simulation

TRIBIC allows to investigate the electric field distribution inside the 3D diamond detector. The transient current signal (TCT) is recorded along with the impact position of a single proton. The analysis of the TCT signal allows to reconstruct the electric field distribution. For a planar electrode configuration the electric field distribution does not vary with the proton impact position and the TCT signal will thus not vary for a perfect detector. In the case of the 3D electrode structure in the square and hexagonal cells, the electric field distribution is non-uniform and

the transient current signal shape is expected to vary as a function of the impact position of the proton in the cell. The complex field structure and resulting TCT signal is simulated and compared to the measurements.

#### 3.2.1 Measurements

Measurements were made on hexagonal and square cells at  $U_b = 20\text{V}$  for positive and negative polarity, with the proton beam incident on the read-out side. A square cell was also investigated at the bias side. Figures 7a and 7b show a comparison of the averaged TRIBIC signal for both square and hexagonal cells at two different field regions within the cells, a high and low field region, as indicated on the plot, on the read-out side. The amplitudes observed are summarised in Table 1.

The amplitude values of the current pulses are about a factor two smaller for low field regions compared to high field regions. The hexagonal cell type has slightly higher amplitude for both regions compared to the cubic cell. These observation can be explained by the field shape and are reproduced by a simulation model explained below. The cumulative integral of the current pulses are shown in Figures 7c and 7d,

| Field | $U_b$ [V] | Cell type | Amplitude [ $\mu$ A] |
|-------|-----------|-----------|----------------------|
| Low   | +20       | Hexagonal | $10.9 \pm 0.8$       |
| Low   | +20       | Square    | $9.4 \pm 0.9$        |
| Low   | -20       | Hexagonal | $12.3 \pm 0.7$       |
| Low   | -20       | Square    | $11.8 \pm 0.9$       |
| High  | +20       | Hexagonal | $25.2 \pm 1.4$       |
| High  | +20       | Square    | $21.2 \pm 0.5$       |
| High  | -20       | Hexagonal | $21.0 \pm 1.2$       |
| High  | -20       | Square    | $19.0 \pm 0.8$       |

**Table 1:** Summary of the amplitude values for TRIBIC measurements at different field values and cell configurations.

the lower amplitude of the the square cell results in a slower rise of the integral compared to the hexagonal cell. The visualization of the maximum amplitude of the current pulses as a function of the incident position of the proton in Figure 8 reveals the variation is related to the electrode geometry. In this figure the cell boundary is indicated by solid line, the electrodes by the open circles, and additionally the low field (open crosses) and high field (open stars) regions used for Figure 7 are indicated. The collection time of the charge signal is strongly dependent on the position and follows the electric field distribution.

TRIBIC measurements were also taken on the bias side of the detector. Figures 9a and 9b show a density plot of the recorded current traces on the readout and bias sides of the detector, respectively. The pulse shapes vary considerably on the readout side of the detector as expected from the amplitude distributions discussed in the previous paragraph. For the bias side the variation is much smaller and a dominant pulse shape is visible, with a FWHM of  $\approx 35$ ns. This can be partly explained by the increased effective electrode resistance experienced by the incident protons; the protons traverse approximately 25% of the diamond thickness (100  $\mu$ m), but the induced charge at the readout electrode sees a path length of ( $\approx 300$   $\mu$ m) to the surface metallization, resulting in an increased RC constant. The RC constant dominates the transient current signal, and thus the amplitude and FWHM of the current signal is independent of the position in the cell as seen in Figures 9c and 9d. From the measurement of

the capacitance and resistance the RC constants was estimated to  $\approx 30$ ns for the bias side measurement which corroborates the observation of no visible significant structure.

### 3.2.2 Simulation

Simulations were carried out using Synopsys TCAD[12] in two (2D) and three spatial dimensions (3D) to understand the observed behavior. Simulations in three spatial dimensions are very CPU intensive and could be run only for a few events. Simulations in two spatial dimensions (2D) are deployed for predictions on a larger area of the detector. For the 2D simulation a mesh representing an area of  $2 \times 2$  square cells was created to include the effects of neighboring cells. Due to the 2D nature of the simulation it is not possible to accurately model a Bragg Peak, however a selection of hits were compared to simulations using a 3D quarter cell mesh to validate that the 2D results are a good approximation to what is obtained with a full 3D simulation.

The 3D simulations were performed using a column resistance of  $175k\Omega$  and a simulated charge density of  $5.882 \times 10^{-5}$  pC  $\mu$ m $^{-1}$  from the diamond surface to a depth of 80  $\mu$ m, and an higher density of  $4.235 \times 10^{-3}$  pC  $\mu$ m $^{-1}$  simulated at a depth between 75 – 85  $\mu$ m to approximate a Bragg peak.

For the 2D simulations the RC constant of the 3D device was adjusted by increasing the resistance for the electrodes, and the simulated charge density was set to  $6.4 \times 10^{-6}$  pC.

A bandgap energy of 5.5eV and a dielectric constant of 5.7 were used in the

simulation[13]. The simulation input parameters for the modelling of the carrier dynamics were for the electron saturation velocity  $v_{s,e} = 9.6 \times 10^6 \text{ cm s}^{-1}$ ; hole saturation velocity  $v_{s,h} = 14.1 \times 10^6 \text{ cm s}^{-1}$ ; low field electron mobility  $\mu_{0,e} = 1714 \text{ cm}^2 \text{ V}^{-1} \text{ s}^{-1}$ ; and low field hole mobility  $\mu_{0,h} = 2064 \text{ cm}^2 \text{ V}^{-1} \text{ s}^{-1}$  [14]. These values are used in a Caughey-Thomas model [15] to calculate the field dependent mobility. To simulate the effect of the amplifier chain, the signal frequency spectrum was limited to 2 GHz corresponding to the bandwidth limit of the current amplifier.

Figure 10 compares simulation and data for the hexagonal and cubic cells in the low high field regions. Shown are the results for a bias voltage of 20V and negative polarity. The agreement of data and simulation is reasonable taking into account the simplification of deploying an effective resistance and the amplifier model. The basic features differentiating the low and high field regions are qualitatively reproduced. The slower turn on of the low field region is visible for both hexagonal and cubic cells. A distinct two peak structure caused by the different time structure of the signal contribution from holes and electrons is resolved in the hexagonal cell low field case in both the simulation and measurement, however it is less pronounced in the case of the simulation.

Figure 11 shows a comparison of the amplitude as a function of position on both hexagonal and cubic cell types. The hexagonal and cubic symmetries are visible, related to the electric field distribution. The amplitude range is comparable to the measurement data shown in Figure 8a and Figure 8c for the hexagonal and cubic cell, respectively. The patterns seen in the amplitude distribution in data and simulation show some differences. The sixfold and fourfold symmetries for the hexagonal and cubic cell are clearly visible, however the shape is not accurately reproduced by the simulation while the amplitude range is comparable.

#### 4. CONCLUSIONS

A 3D diamond detector with square and hexagonal cell geometry was produced with an improved graphitisation process using spherical

aberration corrected laser optics. The detector response to a proton micro-beam was studied. The response to the proton beam is consistent with full charge collection within the active regions of the detector. Significant charge sharing between neighbouring cells has been observed for low bias voltage. The hexagonal geometry shows less charge sharing than the square cells. Transient current measurements have been performed spatially resolved on single 3D diamond detector cells and have been compared to simulations. A significant dependence of the transient current shape on the location in the cell due to the electric field distribution has been observed experimentally and is reproduced with a simulation.

#### ACKNOWLEDGEMENTS

AO would like to acknowledge support from the Royal Society through grant UF120106 and STFC grant ST/M003965/1/. MJB and PSS were supported through a Leverhulme Trust grant (RPG-2013-044). The measurements at RBI were supported by the H2020 project AIDA-2020, GA no. 654168.

#### REFERENCES

- [1] F. Bachmair, L. Bä, P. Bergonzo, B. Caylar, G. Forcolin, I. Haughton, D. Hits, H. Kagan, R. Kass, L. Li, A. Oh, S. Phan, M. Pomorski, D. S. Smith, V. Tyzhnevyyi, R. Wallny, and D. Whitehead, “A 3D diamond detector for particle tracking,” *NIM Phys A* 786, 2015.
- [2] S. Lagomarsino, M. Bellini, C. Corsi, V. Cindro, K. Kanxheri, A. Morozzi, D. Passeri, L. Servoli, C. J. Schmidt, and S. Sciortino, “Radiation hardness of three-dimensional polycrystalline diamond detectors,” *Applied Physics Letters* 106, 2015.
- [3] T. V. Kononenko, M. Meier, M. S. Komlenok, S. M. Pimenov, V. Romano, V. P. Pashinin, and V. I. Konov, “Microstructuring of diamond bulk by IR femtosecond laser pulses,” *Applied Physics A* 90, 2008.

- [4] Newport Corporation, “Spectra Physics Solstice Data Sheet.” [https://assets.newport.com/webDocuments-EN/images/Solstice\\_Ultrafast\\_Laser\\_SP.pdf](https://assets.newport.com/webDocuments-EN/images/Solstice_Ultrafast_Laser_SP.pdf), 2013. [Accessed 07-Nov-2016].
- [5] B. Sun, P. S. Salter, and M. J. Booth, “High conductivity micro-wires in diamond following arbitrary paths,” *Applied Physics Letters*, vol. 105, 2014.
- [6] S. Murphy, M. Booth, L. Li, A. Oh, P. Salter, B. Sun, D. Whitehead, and A. Zadoroshnyj, “Laser processing in 3d diamond detectors,” *Nuclear Instruments and Methods in Physics Research Section A: Accelerators, Spectrometers, Detectors and Associated Equipment*, vol. 845, pp. 136 – 138, 2017. Proceedings of the Vienna Conference on Instrumentation 2016.
- [7] Iia Technologies Pte. Ltd, “Iia Diamond Properties.” <http://2atechnologies.com/2a-diamond-properties/>, 2013. [Accessed 08-Nov-2016].
- [8] M. Shinoda, R. R. Gattass, and E. Mazur, “Femtosecond laser-induced formation of nanometer-width grooves on synthetic single-crystal diamond surfaces,” *Journal of Applied Physics*, vol. 105, no. 5, p. 053102, 2009.
- [9] M. Jakšić, I. Bogdanović Radović, M. Bogovac, V. Desnica, S. Fazinić, M. Karlušić, Z. Medunić, H. Muto, Ž. Pastuović, Z. Siketić, N. Skukan, and T. Tadić, “New capabilities of the Zagreb ion microbeam system,” *NIM Phys B*, 260, 2007.
- [10] J. Ziegler, “Stopping and Range of Ions in Matter.” <http://www.srim.org/>, 2013. [Accessed 01-Nov-2016].
- [11] CIVIDEC Instrumentation, “Current Amplifier Data Sheet.” [https://cividec.at/files/15\\_pdf.pdf](https://cividec.at/files/15_pdf.pdf), 2015. [Accessed 01-Nov-2015].
- [12] Synopsys Inc., “Synopsys TCAD.” <http://www.synopsys.com/home.aspx/>, 2015. [Accessed 28-April-2015].
- [13] L. S. Pan, S. Han, and D. R. Kania, *Diamond: Electronic Properties and Applications*. Kluwer Academic, Dordrecht, 1995.
- [14] H. Pernegger, S. Roe, P. Weilhammer, V. Eremin, H. Frais Kölbl, E. Griesmayer, H. Kagan, S. Schnetzer, R. Stone, W. Trischuk, D. Twitchen, and A. Whitehead, “Charge-carrier properties in synthetic single-crystal diamond measured with the transient-current technique,” *Applied Physics* 97, 2005.
- [15] D. M. Caughey and R. E. Thomas, “Carrier mobilities in silicon empirically related to doping and field,” in *Proc. IEEE vol 52* (IEEE, ed.), 1967.

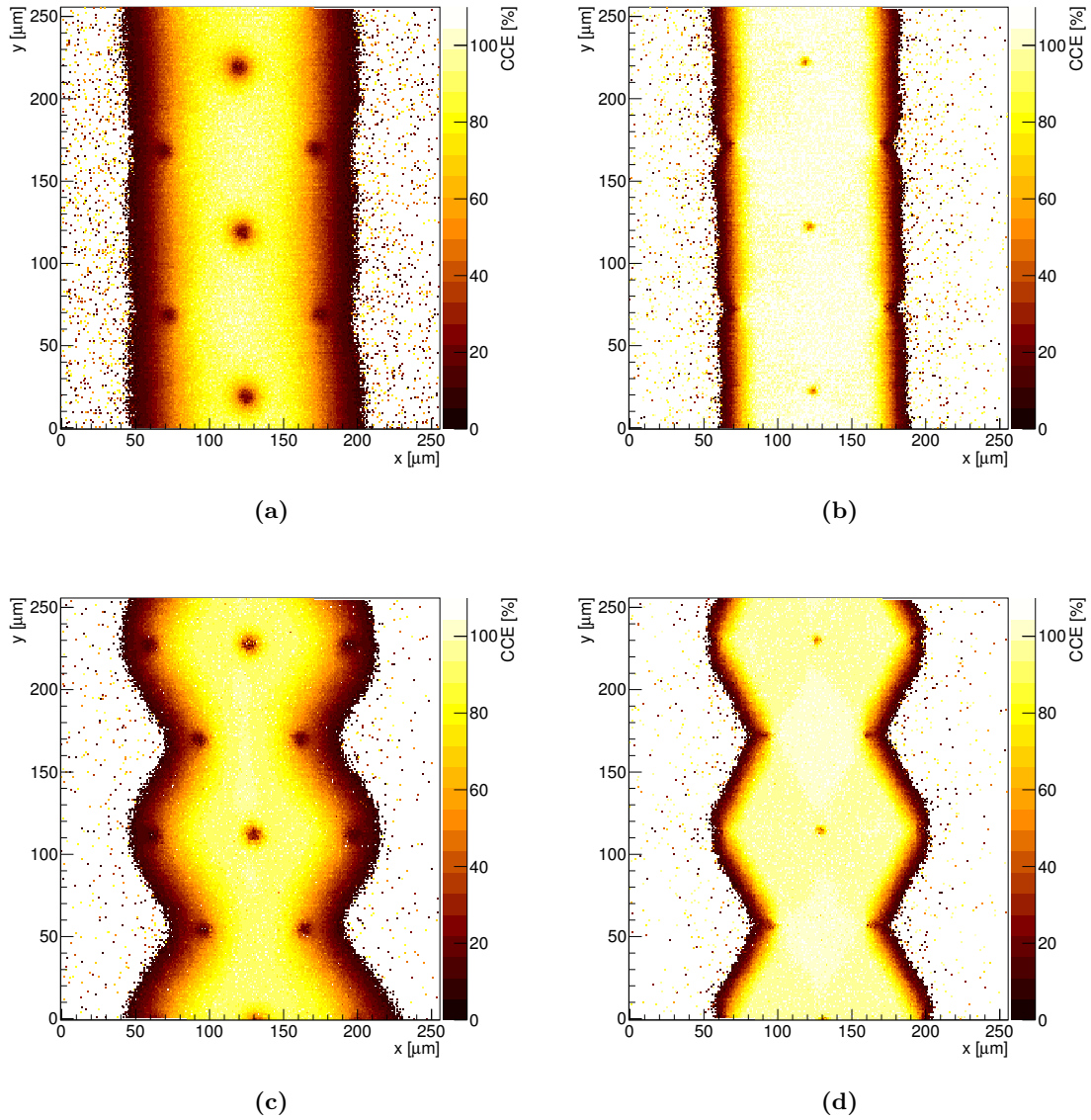


**Figure 3:** Charge collection efficiency (CCE) as a function of position measured with a proton micro-beam for square and hexagonal cells at a bias voltage of  $-2\text{ V}$  and  $-20\text{ V}$ . (a) Square cells at  $-2\text{ V}$ . (b) Square cells at  $-20\text{ V}$ . (c) Hexagonal cells at  $-2\text{ V}$ . (d) Hexagonal cells at  $-20\text{ V}$ .

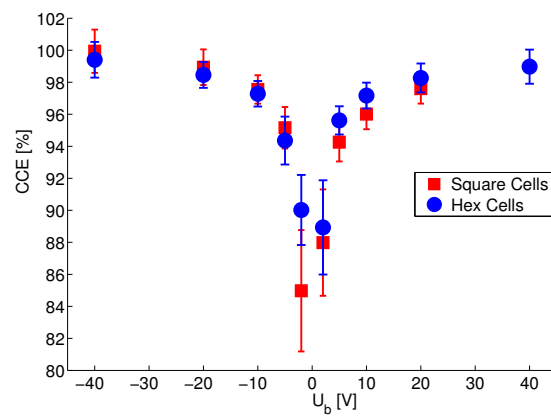


**Figure 4:** Average charge collection efficiency (CCE) as a function of bias voltage for square (red) and hexagonal (blue) cells.

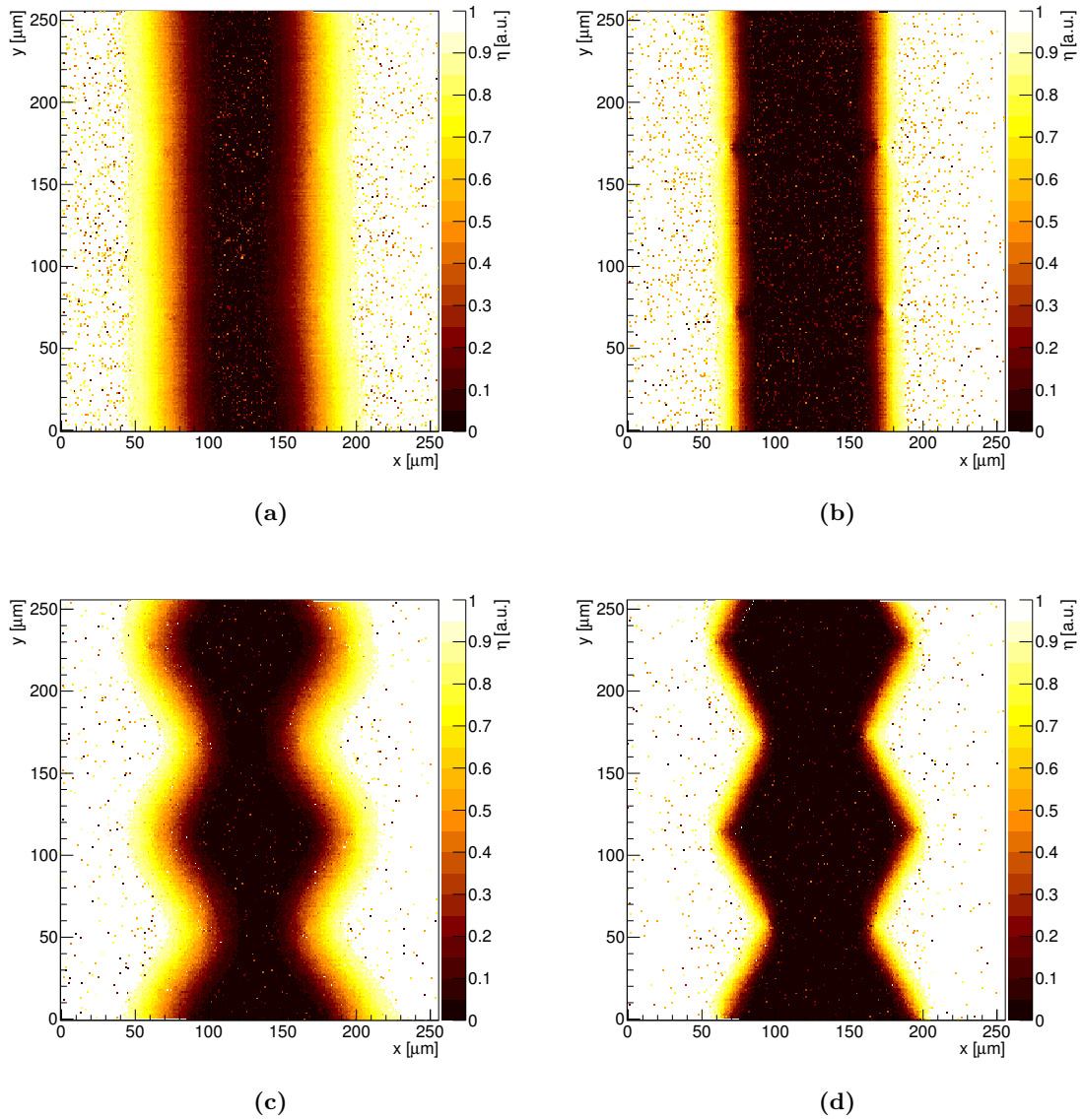


**Figure 5:** Regions of charge sharing between adjacent readout lines for square and hexagonal cells at  $-2\text{ V}$  and  $-20\text{ V}$ . (a) Square cells at  $-2\text{ V}$ . (b) Square cells at  $-20\text{ V}$ . (c) Hexagonal cells at  $-2\text{ V}$ . (d) Hexagonal cells at  $-20\text{ V}$ .

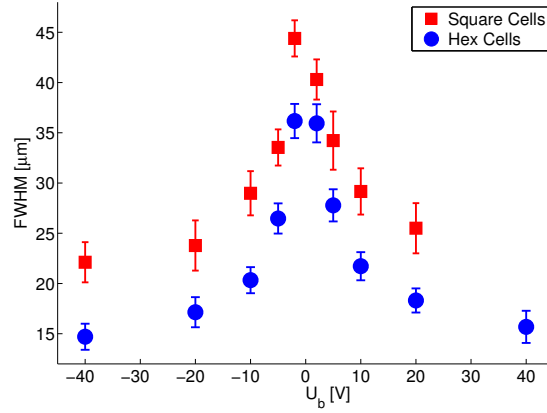


**Figure 6:** The width of the charge sharing regions as a function of bias voltage for square (red) and hexagonal (blue) cells.

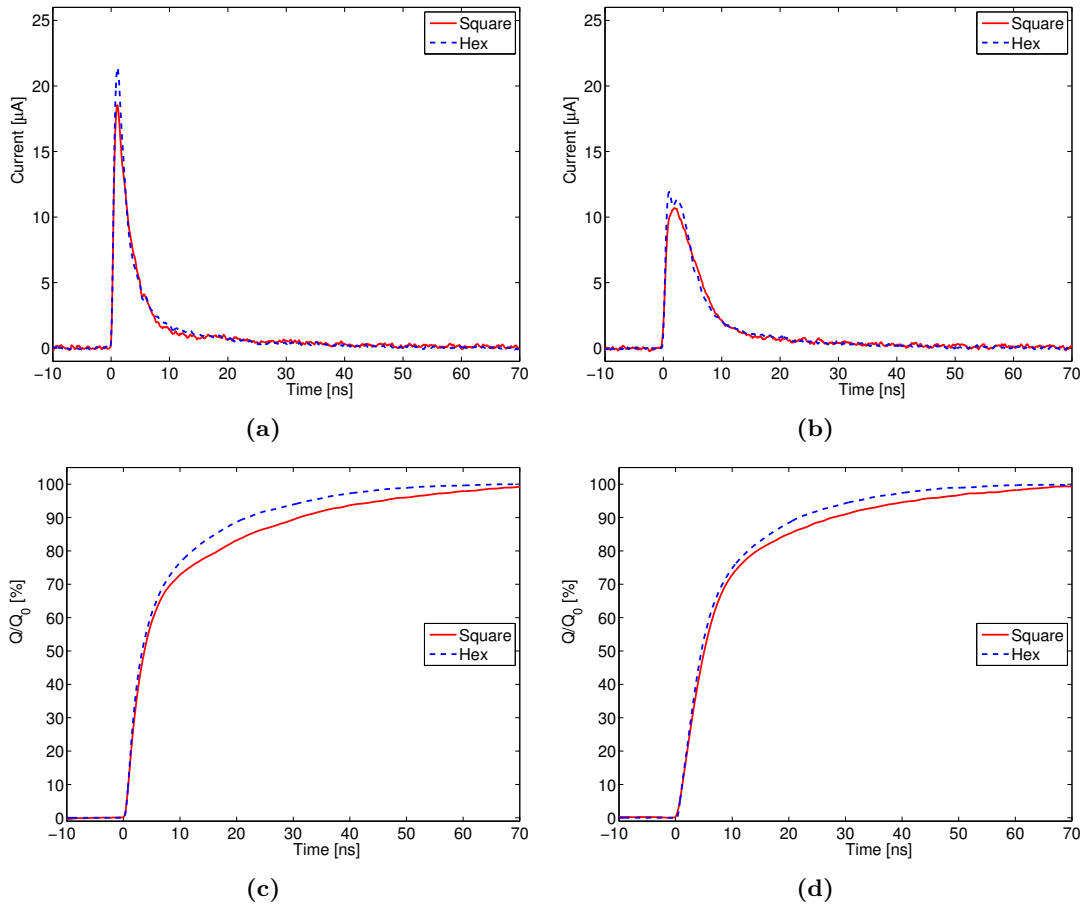


**Figure 7:** Transient current signal from TRIBIC data in (a) a high field region, and (b) a low field region at a bias voltage of  $-20$  V. Cumulative integral of the current pulses are shown in (c) and (d).

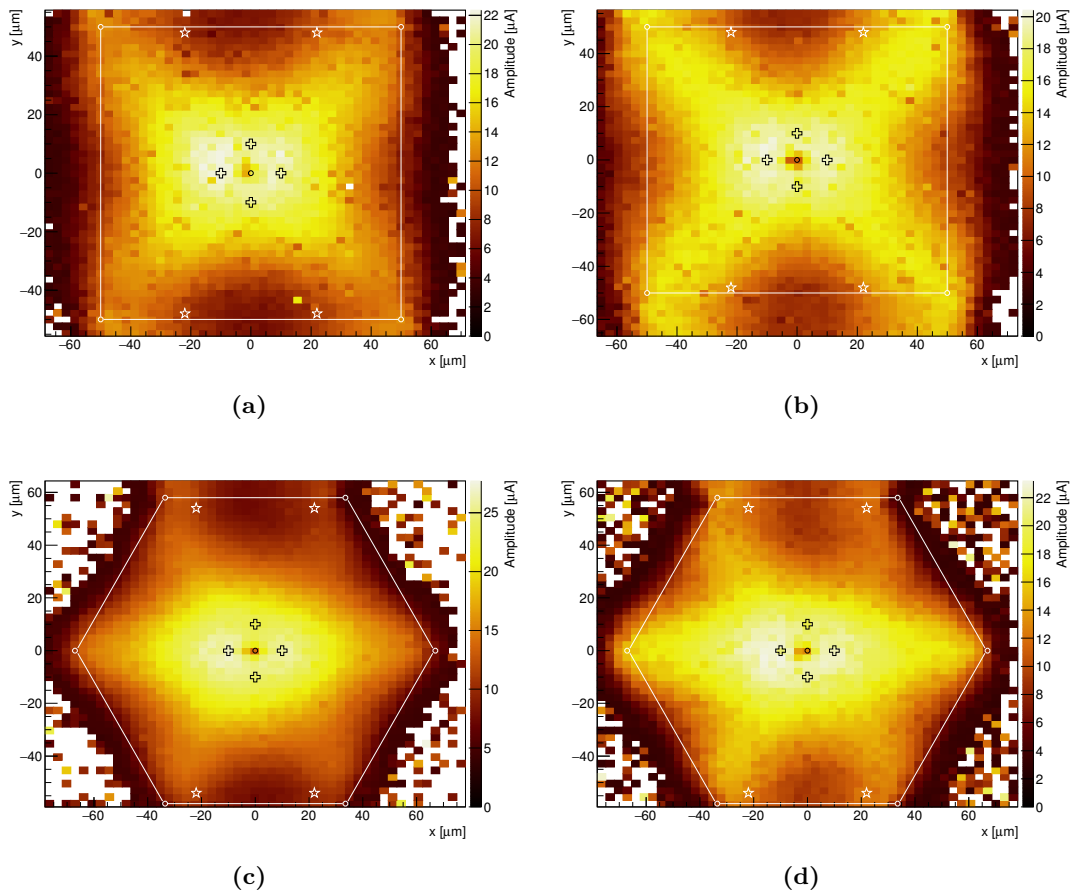


**Figure 8:** Amplitude plots of transient current signals from TRIBIC data at a bias voltage of  $\pm 20$  V. (a) Square cell at +20 V. (b) Square cell at -20 V. (c) Hexagonal cell at +20 V. (d) Hexagonal cell at -20 V. The cell boundary is indicated by the solid lines, the electrodes by the open circles, and additionally the low field (open crosses) and high field (open stars) regions referring to Figure 7 are marked.

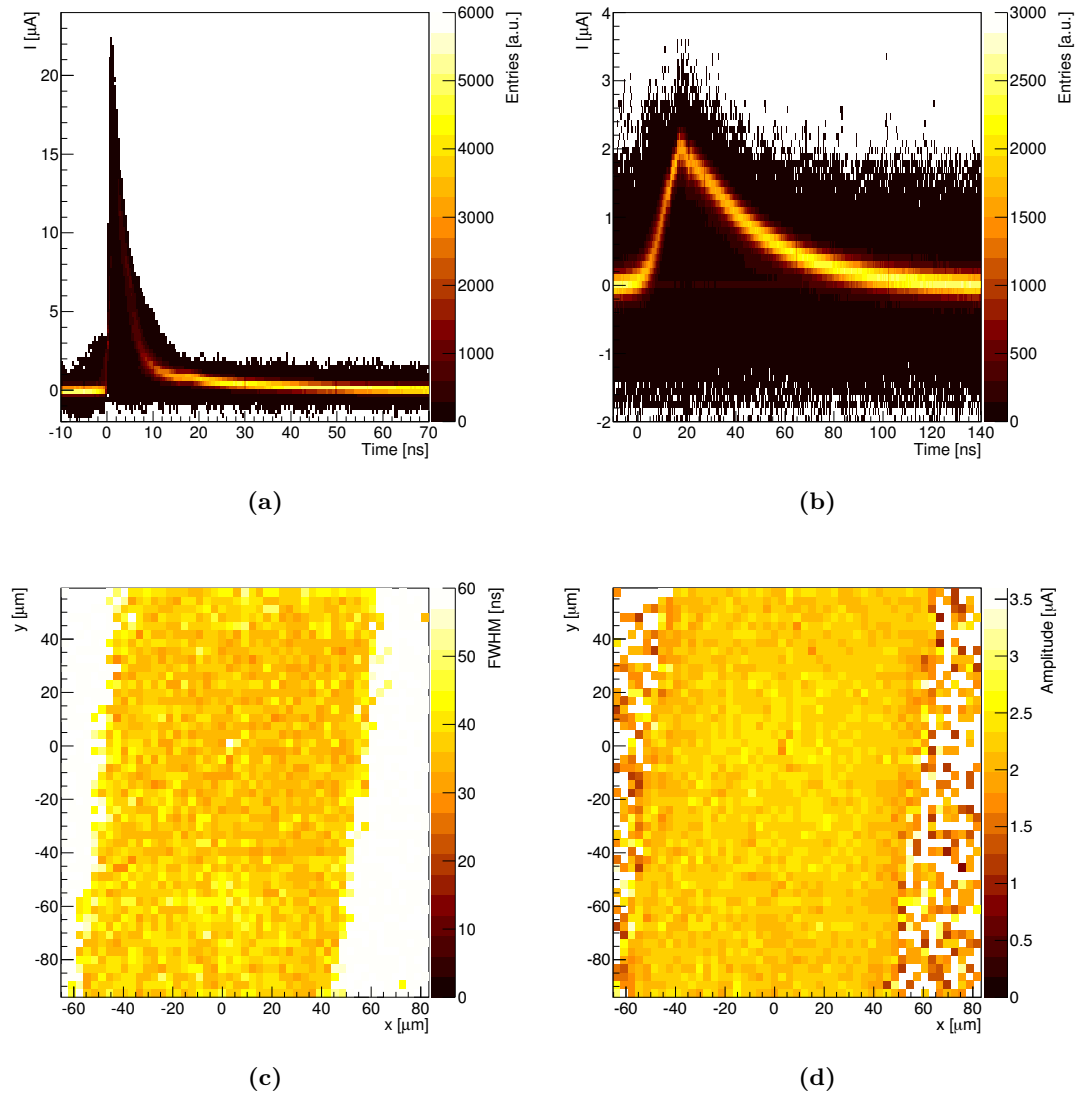


**Figure 9:** A density plot of transient current signals from TRIBIC data for protons incident on (a) the readout side and (b) the bias side of the detector. A 2D plot of the FWHM (c) and maximum amplitude (d) for protons incident on the bias side taken at a bias voltage of +20 V. Note that the tilt has not been corrected in (c) and (d).

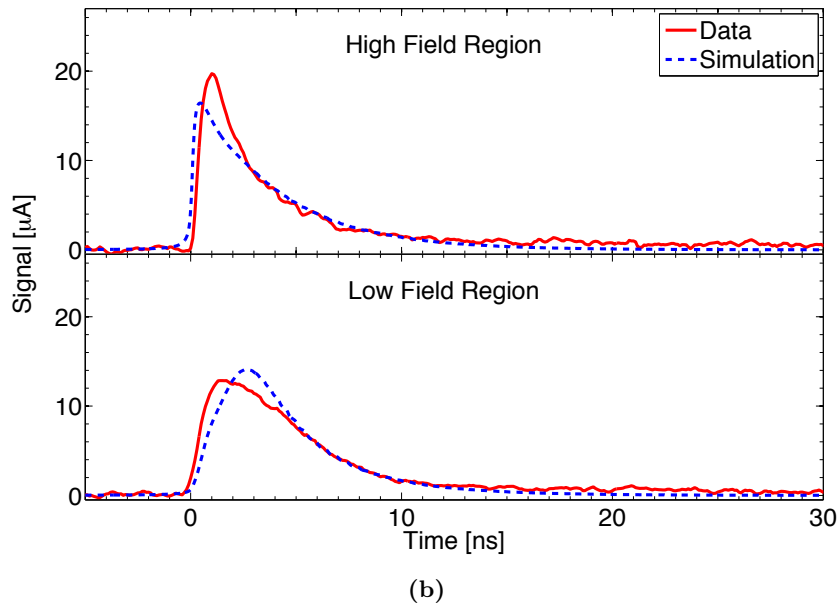
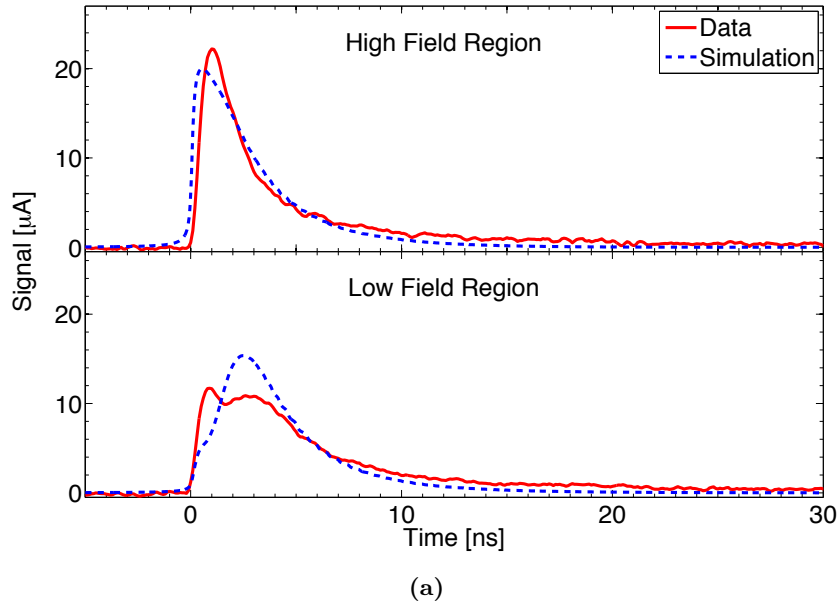


**Figure 10:** Comparison of simulation and data of a TRIBIC signal for the hexagonal (a) and cubic (b) cells in the low high field regions, the proton beam impinging on the read-out side. The results are shown for a bias voltage of -20V.

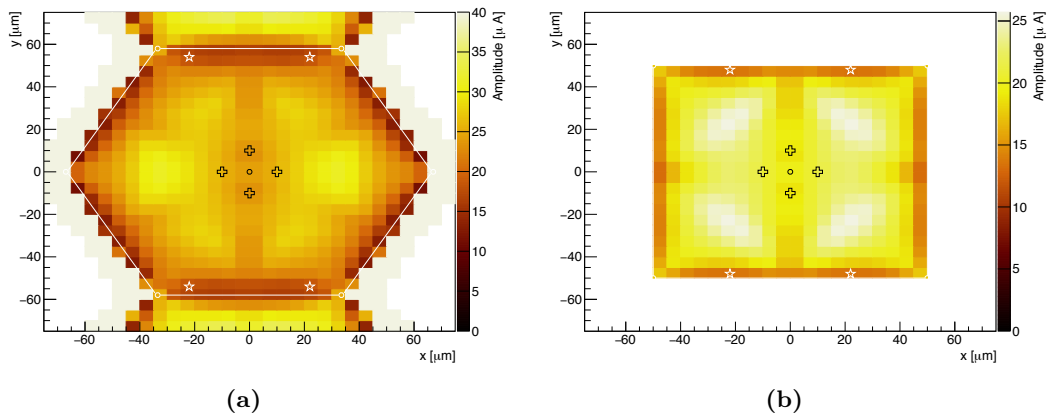


**Figure 11:** Amplitude plots from a simulation of the TRIBIC signal for the hexagonal (a) and cubic (b) cells at a bias voltage of +20V and the proton beam impinging on the read-out side.